

Crawling Waves from Radiation Force Excitation

ZAEGYOO HAH,¹ CHRISTOPHER HAZARD,² YOUNG THUNG CHO¹ DEBORAH RUBENS³
AND KEVIN PARKER¹

¹University of Rochester
Department of Electrical and Computer Engineering
Rochester, NY, 14627
zaegyoo@gmail.com

²GE Global Research
One Research Circle
Niskayuna, NY, 12309

³University of Rochester
Department of Imaging Science
Rochester, NY, 14627

Crawling waves are generated by an interference of two oscillating waves traveling in opposite directions, with a progressive movement resulting from a frequency difference or a phase difference between the sources. While the idea has been applied to numerous applications, all the previous reports used mechanical sources to vibrate the medium. It is shown, through experiments and simulation, that crawling waves can be generated from focused beams that produce radiation force excitation within the tissue. Some examples are also shown.

KEY WORDS: Crawling waves; radiation force; shear speed estimation; sonoelasticity; Young's modulus

I INTRODUCTION

I.1 Review of crawling waves

In a recent discovery, Wu et al^{1,2} used sonoelastography to image slowly-moving interference patterns, termed crawling waves, produced by two opposing shear-vibration sources with a slight difference in frequency. Wu and his colleagues determined that the apparent velocity of the crawling waves is proportional to the underlying local shear velocity, which, in turn, can be used to estimate the elastic modulus of the tissue. The estimation of the local shear velocity was performed using local-frequency estimators, a technique imported from Magnetic Resonance Elastography (MRE).³ Other estimation techniques have been proposed by McLaughlin et al⁴ and Hoyt et al^{5,6} based on arrival times and autocorrelation methods, respectively. Crawling wave sonoelastography has been successfully applied to detect radiofrequency ablated hepatic lesions *in vitro*^{6,7} to characterize human skeletal muscle *in vivo*^{8,9} and to characterize human prostate tissue *ex vivo*.¹⁰⁻¹²

I.2 Advantages of crawling waves

Crawling waves have a number of practical advantages for clinical use and accurate estimation of tissue elastic properties. These are: compatibility with real time Doppler imaging scanners and straightforward, tractable estimators or solutions. In terms of compatibility with existing scanners, crawling waves are adjustable by means of the difference frequency, to accommodate any practical Doppler frame rate. Furthermore, the underlying estimator of Doppler variance is virtually asynchronous with the vibration waves, so there are no special

restrictions on the Doppler pulse-repetition frequency. Equally important, the creation of crawling waves from opposing shear sources sets up a quasi-plane strain condition with the dominant displacement approximately aligned in the axial direction of the scanning transducer, which is the direction of maximum Doppler sensitivity. In this manner, the inherent 2D Doppler imaging sensitivity of conventional scanners is matched to the observation of the shear waves.

Considering solutions and estimations of tissue properties, the crawling wave phenomenon provides a nicely-tractable and convenient set of data for analysis. The basic formulation considers the interference of plane waves from opposing directions. This configuration is relatively straightforward to implement in practice. A variety of sources including small contact surfaces and line sources are capable of creating an approximation of the ideal in a variety of tissues, including muscle, the prostate, breast tissue, the liver and the thyroid.^{1, 8-12} Once the crawling wave pattern is produced and imaged, the estimation of the local elastic modulus and attenuation of the underlying tissue is straightforward. One can fit the data to a mathematical model,⁷ or apply a number of estimators, including local spatial wavelength estimators.^{3,4,6} In addition, methods that have been applied to transient elastography, such as arrival-time analysis, can also be applied to the propagation of the crawling wave nodes, albeit on a much reduced time scale set *a priori* by the selection of the difference frequency. In summary, crawling waves are practical to implement, are highly compatible with the characteristics of conventional Doppler imaging systems and yield straightforward estimates of the local speed or wavelength.

I.3 Generating crawling waves with radiation force

The progressive movement of the crawling wave interference pattern can be realized either in the form of frequency difference or phase difference between sources. As shown in figure 1(a), the mechanical sources with a slight frequency difference generate a slowly-varying interference pattern that would ‘crawl’ across the display of a Doppler imaging scanner. This configuration has been used for applications ranging from homogeneous phantom to *ex-vivo* prostates.⁵⁻¹² In figure 1(b), the same configuration is shown except that the two sources have identical frequency but different phases. Therefore, as the phase changes, either continuously or step-wise, the crawling interference pattern would also be generated.

In applications with commercial ultrasound-imaging systems, however, installing the mechanical sources as part of the system, although possible, might not be practical or attractive. The vibration would start from a surface and, therefore, the influence of overlying layers and propagation losses complicate the measurement. Radiation force, on the other hand, is an alternative to replace the mechanical sources, especially with its controllability and ability to penetrate into deep tissue. Acoustic radiation-force excitation is a second-order effect proportional to the local absorption and intensity and has been utilized in a number of clever configurations for measurement of tissue properties.¹³⁻¹⁹ A system for making local stiffness measurements was introduced by Sugimoto et al in 1990.¹³ Imaging systems employing different aspects of radiation force have been introduced by Fatemi and Greenleaf,¹⁴ Sarvazyan et al,¹⁵ Nightingale et al,¹⁶ Konofagou et al,¹⁷ McAleavey et al¹⁸ and Bercoff et al.¹⁹ However, the use of radiation force creates a number of practical issues for implementation, including acoustic output, penetration depth and timing issue of pushing and scanning. This paper focuses on crawling waves generated from radiation-force excitation.

In section II, we summarize the theoretical background for crawling wave generation and local shear-speed estimation. In section III, the experimental setup is explained and the results will demonstrate the linear superposition of the opposing shear waves. The results will be extended to crawling wave movies on phantoms that will further be analyzed with a shear-speed estimation algorithm.

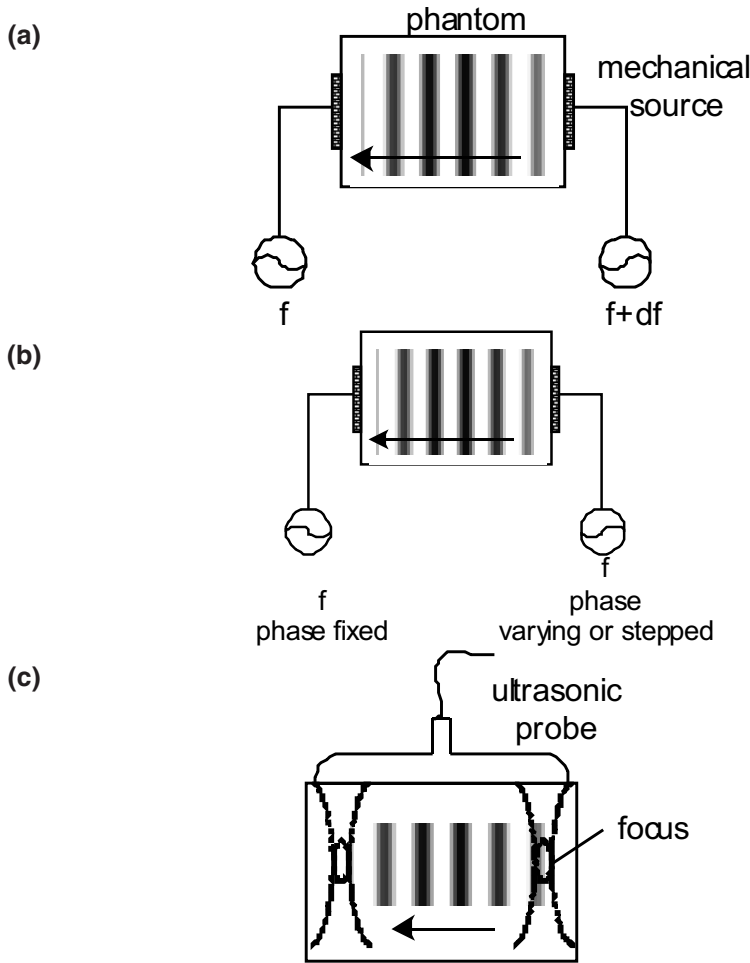


FIG. 1 Generation of crawling waves from mechanical sources with slightly different vibration frequencies (a), same frequency but varying phases (b) and from vibrations induced by radiation force (c).

II THEORY

II.1 Generation of crawling wave movies

Consider the geometry shown in figure 2, where there are two vibration sources with shear waves travelling in opposite directions. If the two sources are vibrating with a slight different frequency, ω and $\omega + d\omega$ respectively, the waves from the left and the right sources, W_{left} and W_{right} , can be simply described as

$$\begin{aligned}
 W_{left} &= A e^{-\alpha x} e^{i(\omega t - kx)}, \\
 W_{right} &= A e^{-\alpha x} e^{i((\omega + d\omega)t - kx - \phi_0)}
 \end{aligned}
 \tag{1}$$

where A is the amplitude, α is the attenuation coefficient of the medium, k is the wave propagation constant and ϕ_0 is the initial phase between the sources. Assuming that any reflection inside the medium or at the boundary is not significant, the square of the amplitude of vibration can be expressed as⁶

$$\begin{aligned}
 \text{amplitude}^2 &= (W_{\text{left}} - W_{\text{right}}) (W_{\text{left}} - W_{\text{right}})^* \\
 &= A^2 e^{-2\alpha x} e^{-2\alpha(D-x)} e^{i(\omega t - 2kx - \phi_0)} e^{-i(\omega t - 2kx - \phi_0)} \\
 &= 2A^2 e^{-\alpha D} \cosh(2\alpha(x - D/2)) \cos(\omega t - 2kx - \phi_0) \quad ,
 \end{aligned}
 \tag{2}$$

where D is the distance between the vibration sources.

Eq. (2) shows that the square of the vibration amplitude has a hyperbolic cosine term that accounts for the attenuation of the medium and a cosine term that are slowly varying with the frequency ω . As a result, crawling waves will be generated that are slowly varying and move from right (higher frequency source) to left (lower frequency source). The hardware required to track this movement, therefore, does not have to be ultrafast and can be implemented with conventional Doppler systems. Furthermore, although Eq. (2) is derived for a homogeneous medium, it has been shown that the local crawling wave properties will reflect the local value of shear wave speed for an inhomogeneous medium.^{1,6}

I.1 Local estimators

Estimators of local tissue stiffness, or shear speed, estimators focus on the $2kx$ term shown in Eq. (2). By extracting the propagation constant k , a function of position, the shear speed c can be estimated. For a fixed time t , after taking care of an attenuation-related hyperbolic-cosine term that is $\cosh(2\alpha(x-D/2))$, the phase difference between two adjacent points x and $x + \Delta x$ would be

$$\begin{aligned}
 \Delta \phi &= 2k \Delta x \\
 \Delta \phi &= 2 \frac{\omega}{c} \Delta x \quad .
 \end{aligned}
 \tag{3}$$

Since the phase difference $\Delta \phi$ can be calculated from the autocorrelation of the analytic signal generated from displacement data, the local estimator will be⁶

$$c = \frac{2 \Delta x}{\tan^{-1}(\text{Im}(R(1)) / \text{Re}(R(1)))} \quad ,
 \tag{4}$$

where $R(1)$ is the autocorrelation of the windowed analytic signal with a shift of one sample. Eq. (4) will generate a map of local shear speed for each frame of the movie, which can be averaged out for better estimation. On the other hand, if we consider a slowly-varying signal at x and $x + \Delta x$, respectively, which corresponds to

$$\begin{aligned}
 \cos(\omega t - 2kx - \phi_0) &\text{ at } x \quad \text{and} \\
 \cos(\omega t - 2k(x + \Delta x) - \phi_0) & \\
 \cos(\omega(t - \Delta t) - 2kx - \phi_0), &\text{ at } x + \Delta x
 \end{aligned}
 \tag{5}$$

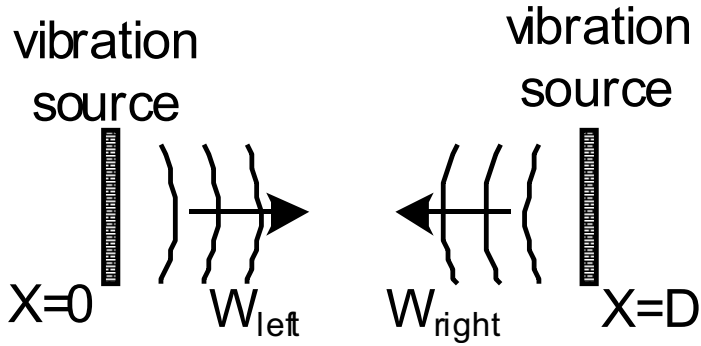


FIG. 2 Basic configuration of crawling wave generation. Two extended sources located at distance D apart from each other continuously vibrate the medium. The measured vibration is the summation of the two propagating shear waves. The square of the amplitude of the displacement is imaged and generates the crawling wave movies.

where the slow time shift is found to be $t = 2kx/c$. The shear speed can be estimated to be

$$c = \frac{2x}{t} \tag{6}$$

Both Eqs. (4) and (6) can be modified for cases where the phase difference, continuous or stepped, rather than the frequency difference generates crawling waves, i.e. with

$$\begin{aligned} W_{left} &= Ae^{-i(t-kx)} \\ W_{right} &= Ae^{-i(t+kx)} \end{aligned} \tag{7}$$

where ϕ is changing. In this case, each frame of the movie is independent and Eq. (4) still applies because Eq. (4) is derived for a fixed frame. Eq. (6) would be modified to be

$$c = \frac{2x}{t} \tag{8}$$

where ϕ is the phase difference measured between the crawling waves at x and $x + \Delta x$.

These derivations assume that vibrations of sources are continuous and sinusoidal. This is typically the case with applications by mechanical sources. In applications employing radiation forces, the ‘pushing’ beam can only apply force unidirectionally, not bidirectionally as in the case of mechanical transducers. Furthermore, in most ultrasound systems, it is desirable to only acquire pulse-echo tracking while the pushing beam is off, due to strong interference effects. As a result, the vibrations at each point of the medium will be pulse-shaped rather than sinusoidal and some processing of the measured data is needed to be able to use Eq. (4) and (8) for local shear-speed estimations. This will be discussed in the next section.

III EXPERIMENTS AND DISCUSSION

If we assume that the system shown in figure 2 is a linear system where the input is the electric-excitation signal and the output is the shear displacements, then the system will ideally show both linearity and shift-invariance as

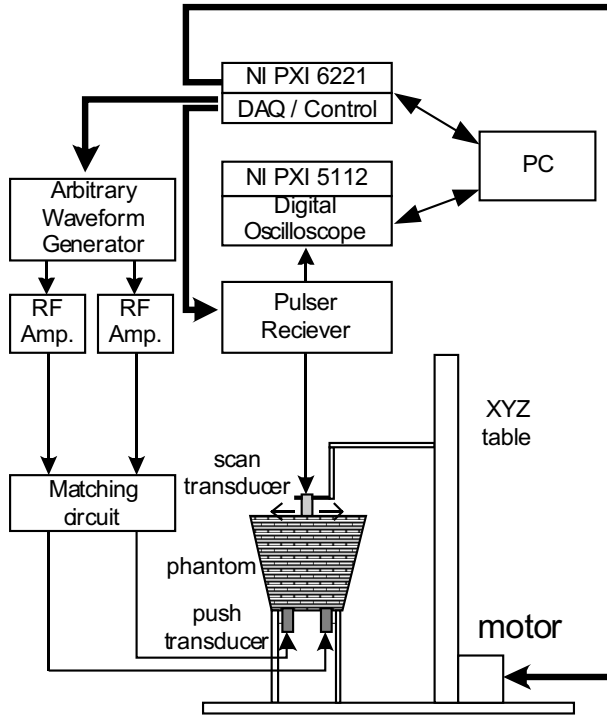


FIG. 3 Experimental setup for verifying the interference of the two shear waves travelling in opposite directions. Two push transducers at the bottom of the phantom exert a radiation force in the medium. The shear waves are detected by a scan transducer on top.

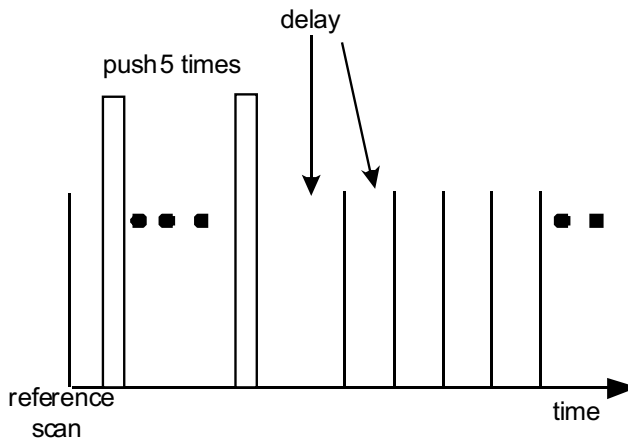


FIG. 4 Timing diagram for ‘push’ and ‘scan’ pulses. The scan starts after a delay to avoid reverberation signals and each scan is distanced by a scan reverb delay.

$$\begin{aligned}
 L[f(t) \quad g(t)] &= F(t) \quad G(t) \\
 L[f(t \quad)] &= F(t \quad) \quad , \tag{9}
 \end{aligned}$$

where $f(t)$ is the excitation signal for the left-side source, $g(t)$ is the excitation signal for the right-side source, $F(t)$ is the displacement due to $f(t)$, $G(t)$ is the displacement due to $g(t)$, is

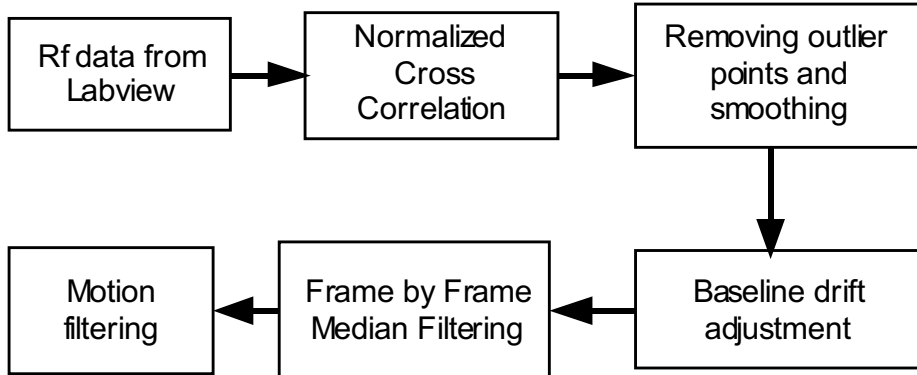


FIG. 5 Signal processing routine to calculate displacement.

the delay and $L[\]$ means the system response. Physically, the linearity will hold for small-strain assumptions; if larger strains were induced, then the system would behave in a more hyperelastic manner that would be nonlinear. In this section, we first show experimental proof for Eq. (9) and then use the property to process the data to generate crawling waves.

III.1 Experimental setup

The experimental setup shown in figure 3 is used. The setup consists of two single element 5 MHz focused transducers (Dakota, focal depth 2 in, diameter 0.75 in) used for radiation-force excitation, one single element 5 MHz scan transducer (Dakota, focal depth 2in, diameter 0.375 in) for pulse-echo measurements, control system (National Instrument NI PXI 1033), pulser/receiver (JSR DPR 300), dual-channel arbitrary-function generator (Tektronix AFG 3022B), broadband power amplifier (Electronics & Innovation A 075) and an xyz table (Velmex, Uni Slide). The control system has three modules: DAQ (Data Acquisition, NI PXI 6221), DSO (Digital Oscilloscope, NI PXI 5112) and AWG(Arbitrary Waveform Generator, NI PXI 5412). A matching circuit is built between the power-amplifier output and push transducers for efficient power delivery. The entire setup is controlled by a PC in a Labview environment.

A gelatin phantom (5% gelatin, 0.15% agar, 1.5% salt with water) is made for this experiment with a speed of sound of 1450m/s and attenuation coefficient of 0.25dB/cm/MHz. The phantom is about 8.9 cm high to ensure that the focal region of the push transducers overlap with that of the scan transducer on top. Since the phantom is low attenuating and the top surface is parallel to the bottom surface, both the push and scan signals exhibit successive reflections that require considerations of the reverberation time. A timing diagram is shown in figure 4. A tone burst of 3000 cycles of 5.25 MHz, which corresponds to a 4% duty ratio of pulse repetition of 70Hz, is generated by the arbitrary-function generator. The frequency of 70 Hz is chosen such that any significant part of the response does not overlap with the responses from the previous excitations. The signal is fed into the power amplifiers and put to the push transducers through the matching circuits. After waiting 350 μ s to avoid any reverb from the pushing excitation, the scan sequence starts with 320 μ s of delay time between them. The scanning rate is, therefore, 3.125 kHz. The push is repeated 5 times to reach the steady state before the scan sequence begins. The sequence is repeated 32 times and the resulting rf signals are averaged to minimize environmental noises. Once the scan is completed at a given scanning position, the scan transducer is moved to next position. The scan is done at 0.5 mm resolution between the center lines of the push transducers, which are 25.5mm apart. The measurement takes about 40 minutes to complete .

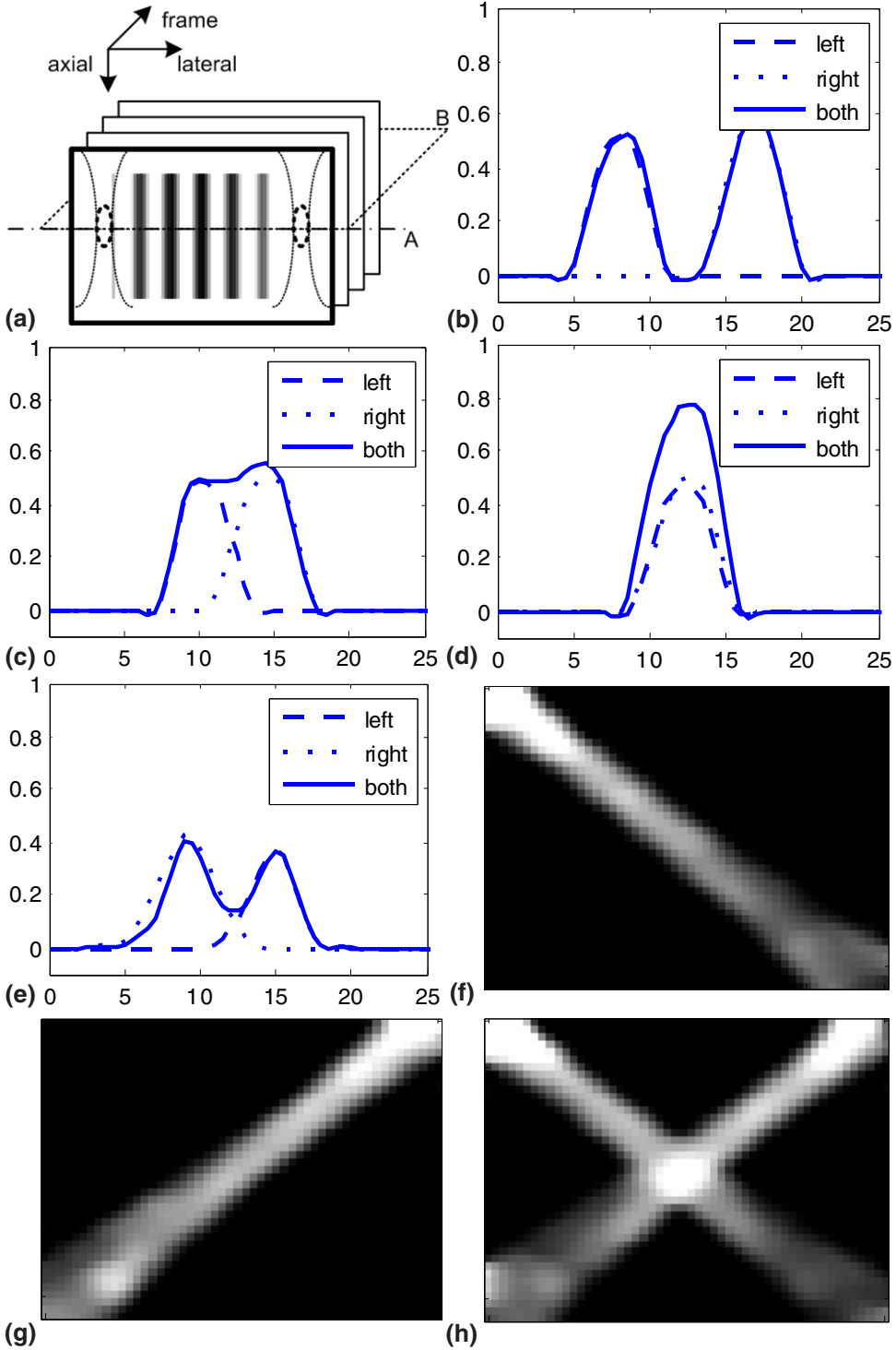


FIG. 6 Processed results of experimental data. (a) To examine the lateral profile, we took a line A at a fixed depth of 3.75 cm from the surface. Similarly, to display the shear-pulse movement, a slice plane B is defined through the 3D data set. (b)–(e) Experimental results along line A at 5.4 ms, 6.68 ms, 7.96 ms and 9.56 ms after the onset of the excitation pulse, respectively. (f)–(h) Image of plane B due to left-side excitation only, right-side excitation only and simultaneous excitation of both sides, respectively.

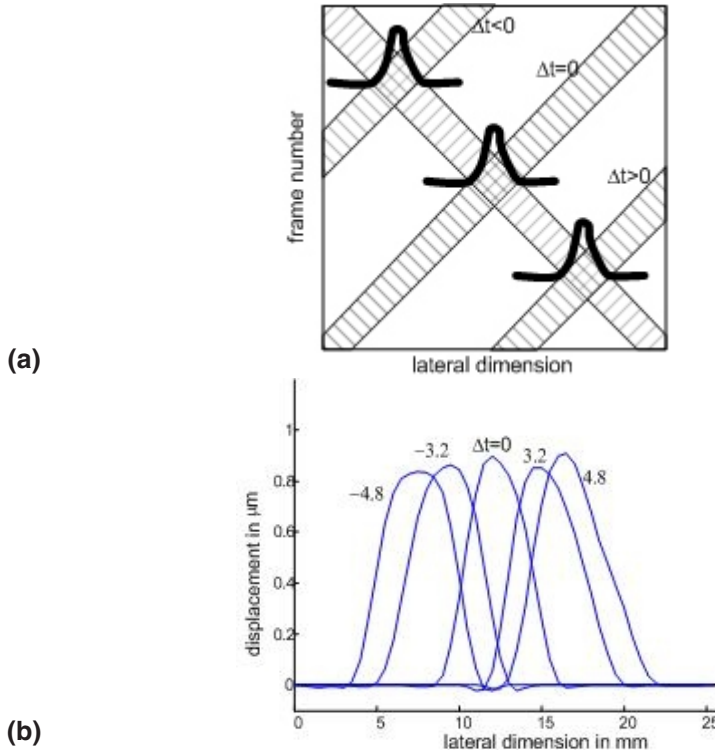


FIG. 7 Movement ('crawling') of shear wave interference. (a) diagram showing the response of shifting one source relative to the other, (b) shifting result from experimental data of figure 6.

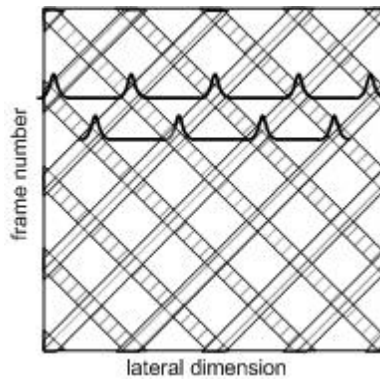


FIG. 8 Diagram explaining simulation of repetitive firing of sources. Firing rate is five times higher than in the case shown in figure 7(a). As the firing rate goes up, more interference pattern will appear.

Three separate experiments are done under identical experimental conditions: exciting left side source only, right side source only and both sources simultaneously.

III.2 Experimental results

The displacement of the phantom is calculated through several procedures explained in figure 5. Following NCC (normalized cross correlation) of the rf data set,²⁰ baseline drift adjustments and smoothing both in the spatial and time domains are performed sequentially.

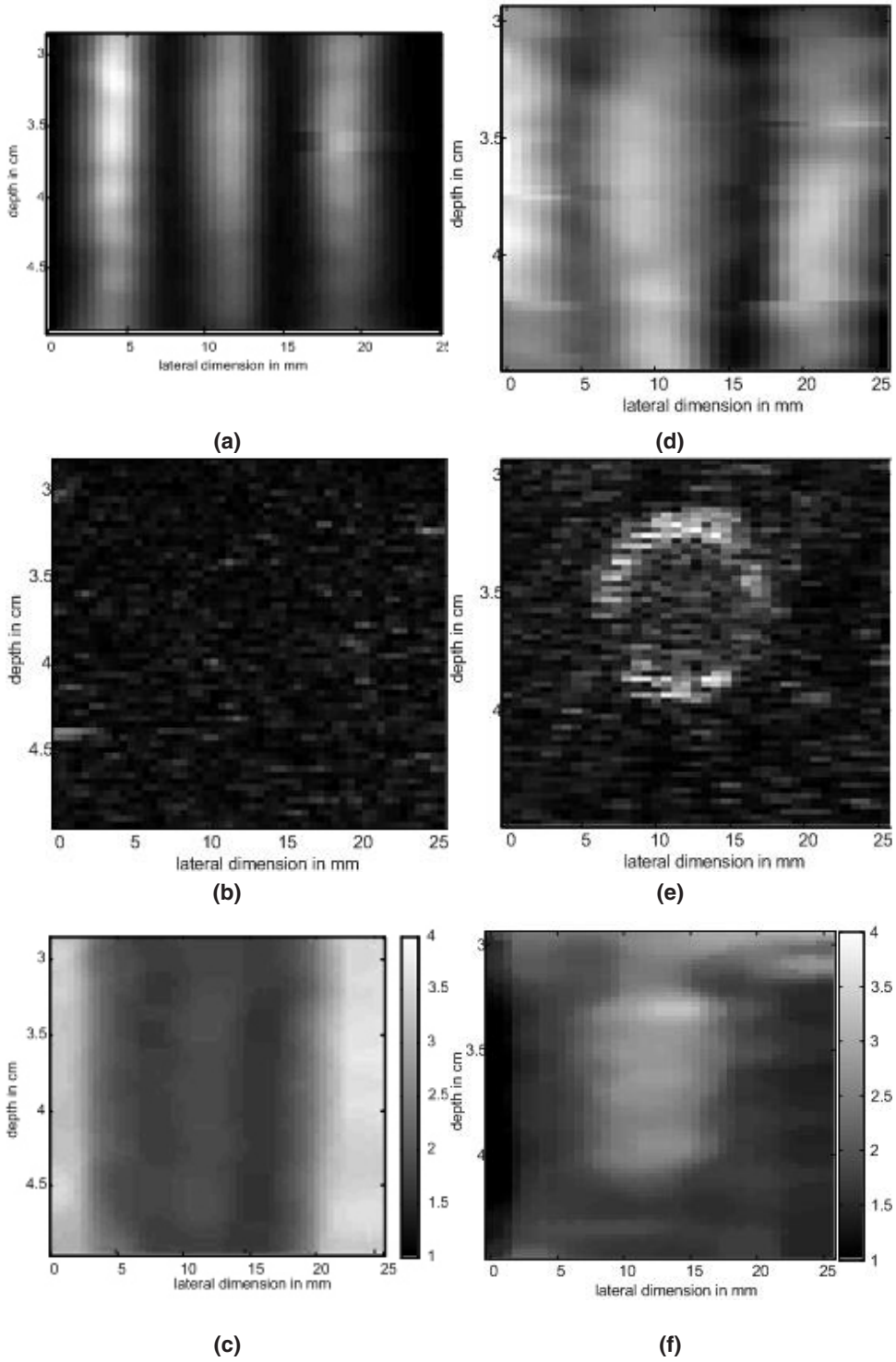


FIG. 9 Generated crawling waves and analysis. Two phantoms are used: one is the same homogeneous phantom used in figure 6 and the other is a phantom with a 6-mm diameter stiff inclusion inside. For the homogeneous phantom, a frame of the generated crawling wave movie is shown in (a), B-mode image in (b) and local shear-speed-estimator result in (c). For the inclusion phantom, on the other hand, a frame of the movie, B-mode image and local shear-speed estimator are shown in (d),(e)and (f), respectively.

Spatial-domain smoothing can be done either with a two-dimensional median filter or with smoothing in axial and lateral directions, where the axial direction is filtered first because it is more slowly varying than the lateral profile. Time-domain smoothing, on the other hand, identifies the expected rise and fall of a propagating wave in the form of a motion filter and removes drifts and other artifacts. The results are shown in figure 6. Typical displacements are below 3 μm . Instead of showing all the frames, we will focus on the lateral profile at a fixed depth of 3.75 cm from the top, shown as line *A* of figure 6 (a). Figures 6 (b) to (e) show displacement profiles due to the left-side source only, right-side source only and both sources at 5.4, 6.68, 7.96 and 9.56 ms after the onset of the excitation pulse, respectively. We observe good correspondence in these graphs despite some minor discrepancies. The match is more easily seen in figures 6 (f) to (h), where the images of a plane defined in figure 6 (a), a frame-lateral dimension image with time on the vertical axis, are shown, respectively, for cases of the left-side push only, the right-side push only and simultaneous push of left and right side sources. Further analysis of the image reveals that the shear wave speed is about 1.8 m/s. Also thermal heating is measured at below 2°C.

III.3 Generation of crawling interference pattern

Let us suppose that the excitations of the two pushing transducers, instead of being simultaneous, have some delay between them. Then the position of the constructive interference would no longer be in the middle. Instead it will move as a function of the excitation delay between the sources, as depicted in figure 7(a). The experimental data of figure 6 is shifted and summed together to show the movement of the pulse in figure 7(b).

This scheme can be further extended by examining the repetitive firing of the sources, as illustrated in figure 8. Compared to figure 7(a), figure 8 displays the interference pattern from the firing rate five times higher than that of experiment above. Two crawling waves were generated with this scheme on two phantoms: the homogeneous phantom used above and a second phantom with a small inclusion inside. The inclusion is a cylinder of 6 mm diameter with composition of 10% gelatin, 0.75% cornstarch and 0.9% salt, with an expected shear speed of 4.5 m/s. Generated crawling wave movies were further analyzed with the local shear-speed estimator described in section II. The results are summarized in figure 9. The crawling waves for both phantoms are generated at 210 Hz. For the sake of demonstration, a frame of the generated movie, a B-mode image and shear-speed map for both the homogeneous phantom and the phantom with an inclusion are shown in figure 9. As seen in figure 9(a), the bright stripes representing higher displacements at interfering peaks are straight vertical line in the homogenous phantom while those of the inclusion phantom are slightly curved, which is characteristic of crawling waves near a circular inhomogeneity. The B-mode image shown in figure 9(e) demonstrates the location of the lesion. The estimator explained in Eq. (4) is used to calculate the shear speed. The result is shown in figures 9(c) and (f) for the homogeneous phantom and the inclusion phantom, respectively. In figure 9(c), the shear-speed map is reasonably uniform at about 1.8 m/s except for regions at the extreme left and right side edges. This is likely due to the transient response near the sources. In figure 9(f), on the other hand, the shear-speed map shows a region of higher elastic modulus that matches the corresponding B-mode image of figure 9(e). The background of figure 9(e) matches the speed of 1.8 m/s. Inside the inclusion, however, the estimate is about 3.2 m/s, which is lower than the expected value of 4.5 m/s. This lowered contrast can be attributed to some melting of the inclusion at the time of pouring the surrounding gelatin phantom. This effect renders the inclusion somewhat fused with background medium. Another possibility is that the reflections at the background-inclusion boundary reduce the apparent propagation speed of the interference pattern.

A Logiq 9 (GE) system has been modified to implement the above-mentioned functionality. A transrectal probe capable of forming focuses at 2.5 cm deep and 18 mm apart is installed in the system. Detailed information and experiments thereof will be covered in a separate paper.

IV CONCLUSION

Crawling waves can be generated using acoustic radiation-force excitation and imaged with pulse-echo sequences for analysis of the underlying elastic properties. However, there are practical differences between those crawling waves produced by mechanical vibration sources and those produced by radiation-force excitation. Mechanical sources can be bidirectional, whereas radiation force sources can only push in the direction of the propagating beam. The simplest approximation to a sinusoidal mechanical vibration source would be a radiation force push that is on for 50% and off for 50% of the cycle. However, because of the strong interference between the pushing excitation and the tracking pulses, there is a need to balance the timing sequence between pushing and tracking. Furthermore, transducer heating can also limit the time or duty cycle that can be devoted to the radiation-force excitation. Thus, radiation force excitations will have a limited duty cycle in the time domain. If the beams are highly focused, the source of vibration will be highly localized in the spatial domain as well. Because of these factors, the interference peaks will be shorter in time and space as compared to the case of purely sinusoidal excitation. This, in turn may require higher sampling rates, spatially and temporally, in order to accurately track the interference peaks. Another limitation of radiation force excitation is in the relatively low (μm range) displacements that are effected with conventional imaging transducers and FDA limits. Nonetheless, some clinical targets that are deep, or relatively inaccessible to compression or vibration sources, may be excited with crawling waves generated by radiation-force excitation.

ACKNOWLEDGEMENTS

This work was supported by NIH Grant 5R01AG016317-07. Helpful discussions with Dr. Wu Zhe at GE are gratefully acknowledged.

REFERENCES

1. Wu Z, Taylor LS, Rubens DJ, Parker KJ. Sonoelastographic imaging of interference patterns for estimation of shear velocity of homogeneous biomaterials, *Phys Med Biol* 49, 911-922 (2004).
2. Wu Z, Hoyt K, Rubens DJ, Parker KJ. Sonoelastographic imaging of interference patterns for estimation of shear velocity distribution in biomaterials, *J Acoust Soc Am* 120, 535-545 (2006).
3. Muthupillai R, Lomas DJ, Rossman PJ, et al. Magnetic resonance elastography by direct visualization of propagating acoustic strain waves, *Science* 26, 1854-1857 (1995).
4. McLaughlin J, Parker KJ, Renzi D, Wu Z. Shear wave speed recovery using interference patterns obtained in sonoelastography experiments, *J Acoust Soc Am* 121, 2438-2446 (2007).
5. Hoyt K, Parker KJ, Rubens DJ. Real-time shear velocity imaging using sonoelastographic techniques, *Ultrasound Med Biol* 33, 1086-1097 (2007).
6. Hoyt K, Castaneda B, Parker KJ. Two-dimensional sonoelastographic shear velocity imaging, *Ultrasound Med Biol* 34, 276-288 (2008).

7. Zhang M, Castaneda B, Wu Z, et al. Congruence of imaging estimators and mechanical measurements of viscoelastic properties of soft tissues, *Ultrasound Med Biol* 33, 1671-1631 (2007).
8. Hoyt K, Castaneda B, Parker KJ. Muscle tissue characterization using quantitative sonoelastography: preliminary results, in *Proc IEEE Ultrasonics Symp*, pp. 365-368 (2007).
9. Hoyt K, Kneezel T, Castaneda B, Parker KJ. Quantitative sonoelastography for the in vivo assessment of skeletal muscle viscoelastography, *Phys Med Biol* 53, 4063-4080 (2008).
10. Castaneda B, Hoyt K, Zhang M, et al. Prostate cancer detection based on three dimensional sonoelastography, in *Proc IEEE Ultrasonics Symp*, pp. 1353-1356 (2007).
11. Hoyt K, Parker KJ, Rubens DJ. Sonoelastographic shear velocity imaging: experiments on tissue phantom and prostate, in *Proc IEEE Ultrasonics Symp*, pp. 1686-1689 (2006).
12. Castaneda B, An L, Wu S, et al. Prostate cancer detection using crawling wave sonoelastography, in *Proc SPIE* 7265, pp. 726513-1-726513-10 (2009).
13. Sugimoto T, Ueha S, Itoh K. Tissue Hardness Measurement Using The Radiation Force of Focused Ultrasound, in *Proc IEEE Ultrasonic Symp*, pp.1377-80 (1990).
14. Fatemi M, Greanleaf JF. Ultrasound-simulated vibro-acoustic spectrography, *Science* 280, 82-85 (1998).
15. Sarvazyan AP, Rudenko OV, Swanson SD, et al. Shear wave elasticity imaging: A new ultrasonic technology of medical diagnosis, *Ultrasound Med Biol* 24, 1419-1435 (1998).
16. Nightingale KR, Palmeri ML, Nightingale RW et al. On the feasibility of remote palpation using acoustic radiation force, *J Acoust Soc Am* 110, 625-634 (2001).
17. Konofagou E, Hynynen K. Localized harmonic motion imaging: theory, simulations and experiments, *Ultrasound Med Biol* 29, 1405-1413 (2003).
18. McAleavey S, Menon M, Orszulak J. Shear-modulus estimation by application of spatially-modulated impulsive acoustic radiation force, *Ultrasonic Imaging* 29, 87-104 (2007).
19. Bercoff J, Tanter M, Fink M. Supersonic shear imaging: A new technique for soft tissue elasticity mapping, *IEEE Trans Ultrason Ferroelec Freq Contr* 51, 396-409 (2004).
20. Viola F, Walker WF. A comparison of time-delay estimators in medical ultrasound, *IEEE Trans Ultrason Ferroelec Freq Contr* 50, 392-401 (2003).